PLEASE CITE THIS ARTICLE AS DOI: 10.1063/5.0135730

AIP Publishing

Nucleation Kinetics Model for Primary Crystallization in Al-Y-Fe

Metallic Glass

Tianrui Duan^a, Ye Shen^a, Seth D. Imhoff^b, Feng Yi^c, Paul M. Voyles^a, John H. Perepezko^a*

- ^a Department of Materials Science and Engineering, University of Wisconsin-Madison, Madison, WI, 53706, USA
- ^b Materials Science and Technology Sigma Division, P.O. Box 1663, M.S. G770, Los Alamos National Laboratory, Los Alamos, NM, 87545, USA
- ^c Nanolab Technologies Inc., Milpitas, CA, USA
- *Corresponding author, perepezk@engr.wisc.edu

Abstract

The high density of aluminum nanocrystals (>10²¹ m⁻³) that develop during the primary crystallization in Al based metallic glasses indicates a high nucleation rate (~10¹⁸ m⁻³s⁻¹). Several studies have been advanced to account for the primary crystallization behavior, but none have been developed to describe the reaction kinetics completely. Recently, structural analysis by fluctuation electron microscopy (FEM) has demonstrated the presence of the Al-like medium range order (MRO) regions as a spatial heterogeneity in as-spun Al₈₈Y₇Fe₅ metallic glass that is representative for the class of Al based amorphous alloys which develop Al nanocrystals during primary crystallization. From the structural characterization, an MRO seeded nucleation configuration is established whereby the Al nanocrystals are catalyzed by the MRO core to decrease the nucleation barrier. The MRO seeded nucleation model and the kinetic data from the delay time (τ) measurement provide for a full accounting of the evolution of the Al nanocrystal density (N_v) during the primary crystallization under isothermal annealing treatments. Also, the calculated values of the steady state nucleation rates (J_{ss}) predicted by the nucleation model agree with the experimental results. Moreover, the model satisfies constraints on the structural, thermodynamic and the kinetic parameters such as the critical nucleus size, the interface energy and the volume free energy driving force that are essential for a fully self-consistent nucleation kinetics analysis. The nucleation kinetics model can be applied more broadly to materials that are characterized by the presence of spatial heterogeneities.

Keywords: Metallic Glasses; Nucleation kinetics; Nanostructured materials; Crystallization

PLEASE CITE THIS ARTICLE AS DOI: 10.1063/5.0135730

1. Introduction

Aluminum based metallic glasses (Al>80 at. %) have received a high degree of attention due to their potential in applications requiring high strength and relatively low density^{1,2}. The specific strength of the as-quenched glass can be further increased to levels beyond that of many common steels through the partial devitrification during the primary crystallization, which produces a high density (10²⁰/m³ up to 10²⁴/m³) of nano-sized aluminum crystals (5-50 nm in diameter)³. Also, the residual amorphous matrix is hardened from the solute enrichment associated with the primary crystallization reaction^{4,5}. The enhanced properties can be optimized by controlling the nanocrystal number density and size distribution within the glassy matrix⁶. At the same time, the restricted growth of the Al nanocrystals allows for the measurement of nucleation rates with limited interference from growth, which makes the Al-based glasses a good system for fundamental nucleation studies.

The high number density of nanocrystals in Al-based amorphous alloys upon devitrification is unusual in comparison to other crystallization reactions. First, typical amorphous alloy compositions are hypereutectic and the thermodynamic driving free energy for crystallization favors intermetallic phase nucleation compared to a primary Al phase by a significant margin⁷. Thus, the selection of Al as the primary crystallization phase must be promoted by a nucleation catalyst to provide a significant kinetic advantage. Second, the primary nucleation yields a high density of extremely small crystals, which further indicates a high nucleation rate and a relatively slow growth velocity. The proposed "phase separation" and "quenched-in nuclei" models were put forward to explain this phenomenon. In the "phase separation" model it is claimed that there is an underlying phase separation step prior to the crystallization, during which the Al-rich and the solute-rich amorphous phases form^{8–11}. However, the large negative enthalpy of mixing in

PLEASE CITE THIS ARTICLE AS DOI: 10.1063/5.0135730

amorphous Al alloys does not favor phase separation. On the other hand, the "quenched-in nuclei" model proposes that there are crystal embryos formed in the undercooled liquid during the rapid quenching, but due to the rapid viscosity increase with the decreasing temperature, there is not enough time for them to grow into crystals^{12–15}. A common feature of both models is that the asspun Al amorphous alloys are spatially heterogeneous, but the origin of the heterogeneities is different between the two models¹⁶. Some related work shows that heterogeneities were found in an as-quenched sample ^{17–20}. Direct evidence for the presence of Al-rich regions in an as-quenched Al₈₅Ni₁₁Y₄ amorphous alloy was provided in the analysis of the ²⁷Al signal in NMR (nuclear magnetic resonance) scans ²¹. In addition, there have been a number of computational studies that are related to the development of spatial heterogeneities in undercooled liquids and glasses and their effect on nucleation russel 22–34.

Fluctuation electron microscopy (FEM) experiments on Al-based glasses show that the structural heterogeneities exhibit diffraction from the {111} and {200} reflections of fcc Al ³⁵but the higher angle / smaller d-spacing diffraction is strongly damped by disorder³⁶. This disordered fcc structure has been variously described as "Al-like", "defective Al", or "disordered Al". In between the strongly diffracting Al-like regions is a more disordered, less strongly diffracting structure which incorporates the rare earth and transition metal elements. In a recent unpublished work³⁷, FEM data and electron scattering simulations were used to determine the mean size and volume fraction of the Al-like regions in Al₈₈Y₇Fe₅ and related alloy. It was suggested that the Alrich regions can act to promote the nanocrystallization. Similar reports of quenched-in precursor structures were observed from Al-Y-Ni-Co amorphous alloys including the effects of minor solute additions of Cu, Pd and Nd in altering the crystallization behavior to yield an ultra-high Al nanocrystal density of about 10²⁴ m⁻³ 38,39.

PLEASE CITE THIS ARTICLE AS DOI: 10.1063/5.0135730

However, the existing framework of the kinetic theory for both the nucleation and growth reactions treats the transforming matrix as a medium with a uniform structural arrangement, and a uniform supersaturation or undercooling ⁴⁰. It is evident that kinetic models that are based on a uniform structure, such as the popular Johnson-Mehl-Avarmi (JMA) approach, do not represent the kinetic influence of structural heterogeneities quantitatively and will not reveal insights into transformation behavior ⁴¹. Indeed, the role of structural heterogeneities was highlighted recently by Gupta et al ⁴² in their analysis of crystal nucleation in an oxide melt. Therefore, it is necessary to utilize the characteristics of the aluminum-like (MRO) spatial heterogeneities as the basis for the kinetic model to describe the initial Al nanocrystal nucleation. The structural characteristics determined in previous work³⁷ are combined with the Al nanocrystal nucleation measurements as the basis for an MRO catalysis nucleation model for an Al₈₈Y₇Fe₅ metallic glass that is representative for the class of Al-base amorphous alloys which develop Al nanocrystals during primary crystallization.

In addition to the recognition of the importance of spatial heterogeneities on the nucleation reaction, it has been demonstrated that there can exist different pathways involving precursor reactions leading up to the final nucleation product structure. ^{43–45}The different pathways have been observed in studies of electrolyte solutions and have been called non-classical pathways since they are not well described by classical nucleation theory (CNT). At the same time studies of the crystallization of glasses or undercooled liquids have demonstrated the validity of CNT^{46–48}.

2. Experimental procedure

Ingots of Al₈₈Y₇Fe₅ (at. %) alloys were produced by arc melting of pure components (99.999% Al, 99.98% Y and 99.99% Fe) five times to ensure homogeneity. Ribbons were formed

PLEASE CITE THIS ARTICLE AS DOI: 10.1063/5.0135730

by single roller melt spinning on a copper wheel with a tangential speed of 55 m/s, corresponding to an approximate cooling rate of about 10⁵ K/s. Both the arc melting and melt spinning were performed in an inert argon atmosphere. The structure of the ribbons was examined by X-ray diffraction (XRD) with Cu Kα radiation. A Perkin Elmer Diamond DSC was used for the isothermal annealing and continuous heating investigations. Before the isothermal treatments, samples were heated to 200°C at a heating rate of 250 K/min and then to the targeted temperatures (237°C, 240°C, 245°C, and 247°C) at 20 K/min to minimize the temperature overshoot. The isothermal annealing temperatures were chosen so that the number of the Al nanoparticles is neither too large nor too small to be counted accurately from the TEM images. After the isothermal treatments, the samples were rapidly cooled to the room temperature at -250 K/min. The fast heating and cooling rates were used to avoid the crystallization during the heating and cooling steps. The non-isothermal runs were performed under a constant heating rate of 20 K/min. The DSC was calibrated with standard In and Pb samples at 20 K/min prior to experiments.

TEM specimens were prepared by electro-polishing in a 25/75 vol.% nitric acid/methanol mixture at -50°C~-40°C. The number of Al nanocrystals was counted from a series of bright field (BF) and dark field (DF) images. The BF images were taken at three different areas on each sample. Several DF images of the same area were taken using non-overlapping portions of the diffuse diffraction ring and were applied to distinguish the overlapping particles shown on the BF images. The overlap particles are bright on top of the dark particles in DF images. The thicknesses of the samples were measured through FEI Titan EELS (electron energy loss spectroscopy) under the Scanning Transmission Electron Microscopy (STEM) mode based on the log-ratio technique: t/λ = $ln(I_t/I_0)$, where t is thickness, I_t is the total number of electrons incident on the sample, I_0 is the number of unscattered electrons and λ is the scattering mean free path, values ($\lambda_{elastic} = 84 \pm$

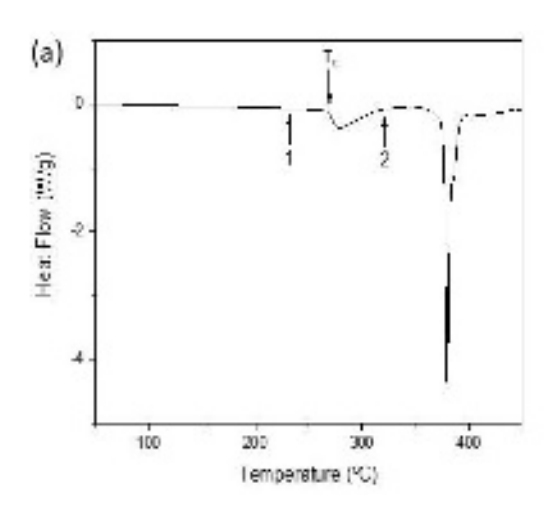
PLEASE CITE THIS ARTICLE AS DOI: 10.1063/5.0135730

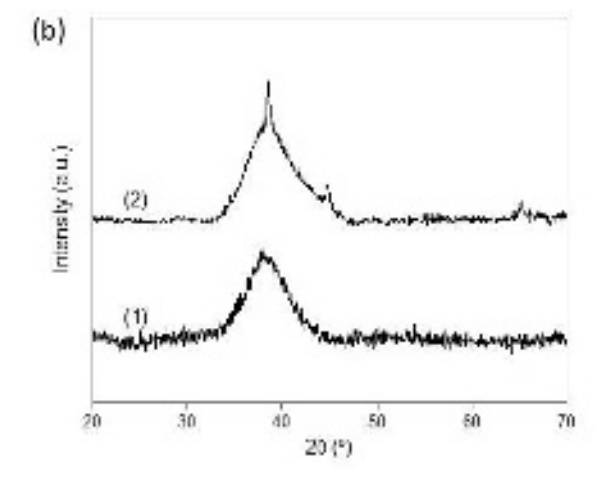
1 nm, $\lambda_{inelastic} = 149 \pm 1$ nm) obtained from the literature ⁴⁹. The thicknesses range from 80 to 110 nm. The nanocrystal number in a given area and the sample thickness yielded the crystal number density values.

3. Results

3.1 Crystallization process during continuous heating treatment

The continuous heating trace for an amorphous Al₈₈Y₇Fe₅ sample at 20 K/min (Fig. 1a) shows the primary crystallization peak with the onset temperature at 540 K (267°C) and the sharp secondary crystallization peak starting at 638 K (365°C). The crystallization products produced at different temperatures were analyzed by XRD (Fig. 1b). Prior to the primary nucleation, the XRD shows an amorphous structure (Fig. 1b, curve 1). During the primary crystallization, the Alfcc phase precipitates as a dispersion of nanocrystals surrounded by a glassy phase (Fig. 1b, curve 2). In summary, the crystallization pathway in Al₈₈Y₇Fe₅ is an initial primary reaction of Al_{fcc} from the matrix followed by the precipitation of intermetallic phases in the remaining sample volume at higher temperatures.





PLEASE CITE THIS ARTICLE AS DOI: 10.1063/5.0135730

Fig. 1 (a) Continuous heating DSC trace (20 K/min) of Al₈₈Y₇Fe₅ metallic glass. The onset temperature for the primary crystallization is at 267°C. (b) The XRD traces corresponding to different annealing products from heating to different labeled temperatures.

The shape of the primary crystallization signal (Fig. 1a) provides an indication of the controlling kinetic behavior. The initial onset of the reaction is sharp and the heat evolution increases with increasing temperature, indicating rapid progress of the reaction. However, after the peak, the rate slows to reveal a large asymmetry in the signal. The main reason for the tail in heat production at higher temperatures has been generally attributed to the increased solute level in the remaining matrix acting to slow the growth rate of the nanocrystal population⁵⁰. The separation as large as 52 degrees between the primary and the secondary crystallization peaks indicates the good stability of the nano-crystallized Al-based metallic glasses.

3.2 Characterization of primary crystallization induced by isothermal heating treatment

Isothermal annealing treatments provide the information such as the number density, crystal size distribution as well as the transient delay time. The details of the heat treatment schedule are shown in Fig. 2a. In order to gain a perspective on the reaction progress with time at a single temperature, a comparison of XRD traces for Al₈₈Y₇Fe₈ samples annealed at 245 °C for various times is given in Fig. 2b. A broad peak, characteristic of an amorphous structure, centered at about the solvent species interatomic distance, is present in all traces. With the increased annealing time, the broad peak at $2\theta=38^{\circ}$ (111) sharpens while peaks at 45° (200) and 65° (220) begin to rise out of the baseline indicating a growing volume fraction of aluminum nanocrystals. The qualitative X-ray information supplements quantitative TEM image analysis. Bright field

TEM images from the samples annealed at the same temperature are given in Fig. 3, showing that the Al particle number density increases with the annealing time.

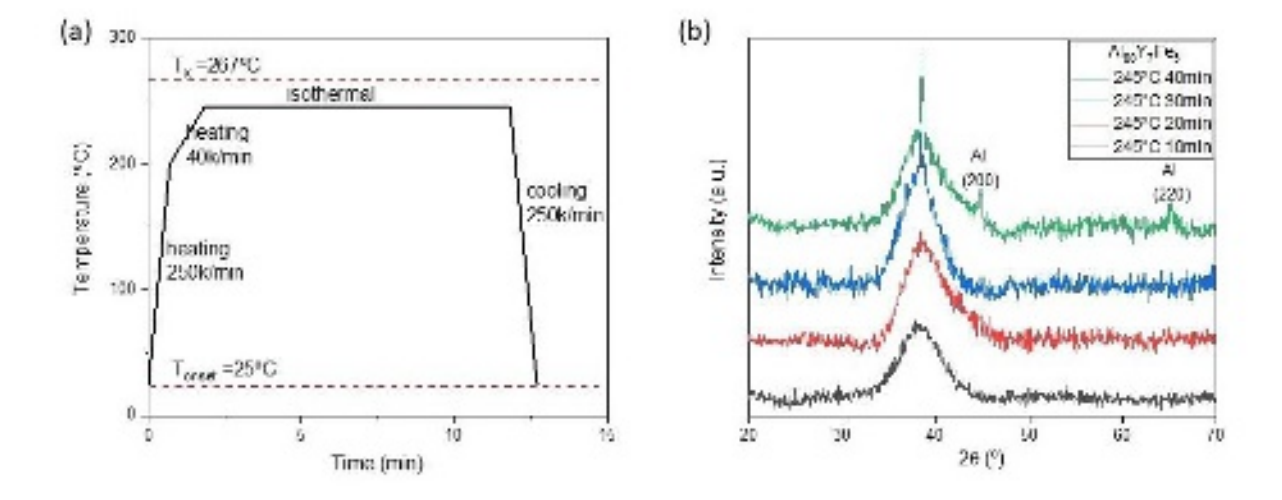


Fig. 2 (a)Schematic illustration for annealing treatments. (b)X-ray traces for Al₈₈Y₇Fe₅ annealed for various times at 245°C.

PLEASE CITE THIS ARTICLE AS DOI: 10.1063/5.0135730

Fig. 3 Bright field TEM for Al₈₈Y₇Fe₅ annealed for various times at 245°C. (a) as quenched, (b) 10 mins, (c) 20 mins and (d) 40 mins.

3.2.1 Particle density analysis

The particle counting on the TEM images and the volume information obtained from the thickness measurement yielded the resulting nanocrystal number density for $Al_{88}Y_7Fe_5$ subjected to isothermal treatment at temperatures ranging from 237°C to 247°C (20 to 30 degrees lower than T_x) for various lengths of time (Fig. 4). An equivalent sphere method is used to quantify the size of the crystal where the crystal is treated as a circle with the same area. The temperature range was chosen so that the transient time was measurably large, but the crystallization reaction occurred over an accessible laboratory timescale. Similar plots have also been obtained by *in situ* x-ray powder diffraction measurement of the relative volume fraction of the crystalline component variation with time 51 or by integrating either the isothermal DSC trace 52 or the NMR spectra 21 . The crystal number density is initially zero but gradually rises during the transient stage, and then

PLEASE CITE THIS ARTICLE AS DOI: 10.1063/5.0135730

reaches a steady state nucleation stage when the nucleation rate is constant and finally saturates at a plateau when the crystal number density stops increasing. The slope of this straight line gives the steady state nucleation rate J_{ss} . With a decrease in annealing temperature, the curves shift to the longer time direction so that the delay time, τ gets longer and the steady state nucleation rate J_{ss} decreases. The coarsening stage, where the crystal number density decreases because the largest crystals grow at the expense of the smallest crystals, is not shown in Fig. 4, since the experimental annealing time was not long enough to reach this stage.

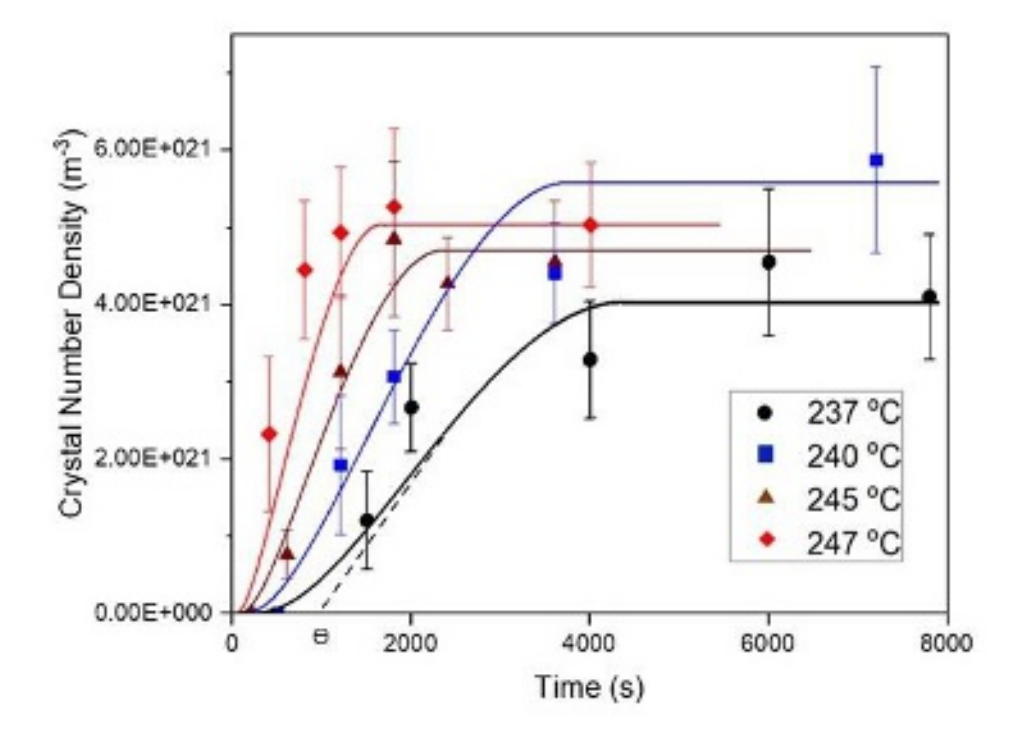


Fig. 4 The experimental (points) and calculated (solid curves) aluminum nanocrystal number density at various temperatures and times for Al₈₈Y₇Fe₅. θ is the intersection of the extrapolation of the nucleation curve and the time axis, which represents induction time.

3.2.2 Particle size evolution

As demonstrated in Fig. 3, the TEM images reveal that initially (10 min to 20 min) the particles grow spherically and after 40 min they begin to grow dendritically. The whole growth

PLEASE CITE THIS ARTICLE AS DOI: 10.1063/5.0135730

process is complex because Al diffuses faster than Fe and Y and at the beginning the diffusion of Al determines the growth rate. However, as the matrix composition changes, the diffusion of Fe and Y are the limiting factors determining the growth rate. The crystal size probability distribution function plots (PDF) obtained from the crystal size cumulative distribution function plots (CDF), for the amorphous Al₈₈Y₇Fe₅ annealed at 245°C for 10 min (Fig. 5a) and 60 min (Fig. 5b) exhibit a bell shape, which indicates transient nucleation ⁵³. According to Fig. 4, the sample will be at the initial period of the steady state stage at 245°C for 10 min, so that the small size classes make up a majority of the overall population in Fig. 5a. However, when the annealing time reaches 60 min at 245°C, the sample is at the saturation stage and therefore the size distribution skews towards large sizes (Fig. 5b). Also, the size distribution spreads in a wider size range for the sample annealed for 60 min than the one annealed for 10 min.

11

This is the author's peer reviewed, accepted manuscript. However, the online version of record will be different from this version once it has been copyedited and typeset. PLEASE CITE THIS ARTICLE AS DOI: 10.1063/5.0135730

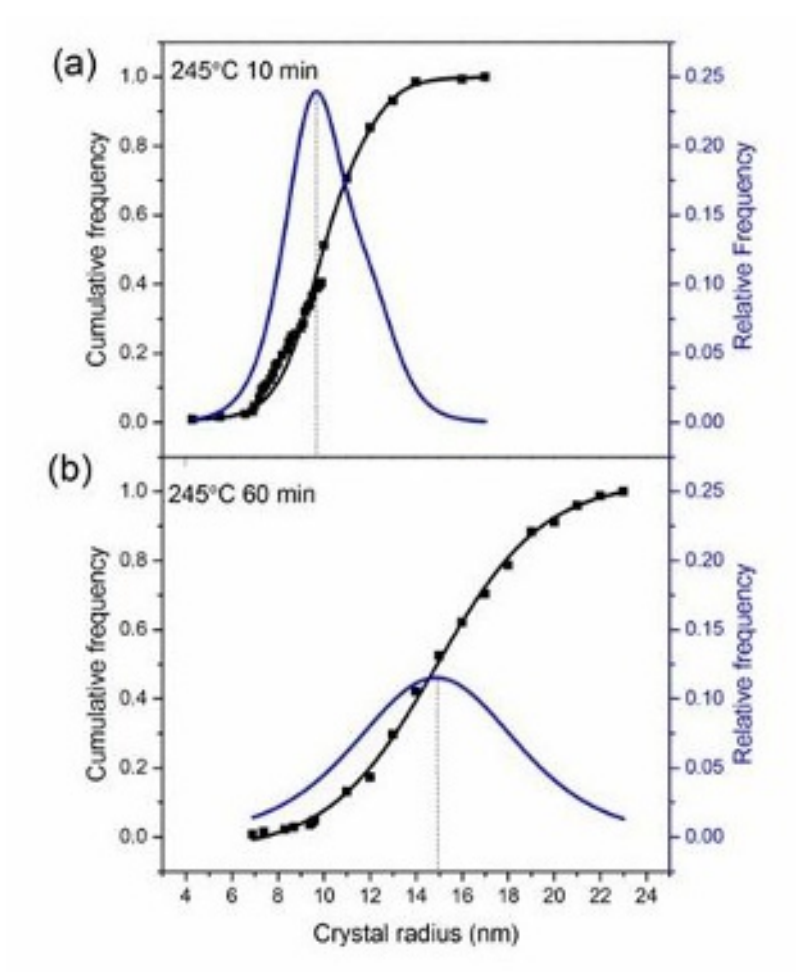


Fig. 5 Al_{fcc} nanocrystal size cumulative and probability distribution functions plots for Al₈₈Y₇Fe₅ annealed at 245°C for (a) 10 min and (b) 60 min.

3.3 Size and density of Al-like regions in as-quenched samples

FEM experiments were conducted on as-quenched Al88Y7Fe5, then compared to electron scattering simulations from atomistic models to determine the size and volume fraction of the Al-like regions. The experiments, and analysis are described in detail elsewhere³⁷, but the primary findings are summarized in the supplemental Material D. The conclusion is that the Allike regions have a mean radius of 0.85 nm and a number density of 5.2×10^{25} m⁻³ in the asquenched glass.

PLEASE CITE THIS ARTICLE AS DOI: 10.1063/5.0135730

This is the author's peer reviewed, accepted manuscript. However, the online version of record will be different from this version once it has been copyedited and typeset

4 Discussion

4.1 MRO seeded nucleation model

In the analysis of the primary crystallization kinetics in amorphous Al based alloys, it is recognized that the MRO regions are present within the melt-quenched amorphous phase as an inherent spatial heterogeneity. Based upon the structural heterogeneity, the crystallization kinetics can be analyzed by classical nucleation theory 54 with the MRO as the heterogenous nucleation site. The steady state nucleation rate can be expressed as:

$$J_{SS} = \rho \beta \mathbf{Z} \exp\left(-\frac{\Delta G^*(r)}{kT}\right) \tag{1}$$

where ρ is the nucleation site density, β is the attachment frequency, Z is the Zeldovich factor accounts for the decay of supercritical clusters, $\Delta G^*(r)$ is the nucleation barrier and k is the Boltzmann constant.

For an idealized spherical cluster with a radius of r, which develops from an MRO region that is also treated as spherical of radius r_0 (Fig. 6), the overall work of cluster formation, $\Delta G(r)$ is obtained as⁵⁵

$$\Delta G(r) = G_{crystal} - G_{amorphous}$$

$$= \left(\frac{4}{3}\pi r^3 \Delta G_V + 4\pi r_o^2 \sigma_{MRO/crystal} + 4\pi r^2 \sigma_{crystal/glass}\right) - \left(\frac{4}{3}\pi r_o^2 \Delta G_V + 4\pi r_o^2 \sigma_{MRO/glass}\right)$$

$$= \frac{4}{3}\pi (r^3 - r_o^3) \Delta G_V + 4\pi (r^2 - r_o^2) \sigma_{crystal/glass} + 4\pi r_o^2 \sigma_{MRO/crystal}$$
(2)

where ΔG_v is the volumetric driving free energy, $\sigma_{crystal/glass}$ is the nanocrystal-glass interfacial energy, $\sigma_{MRO/crvstal}$ is the MRO-nanocrystal interfacial energy and $\sigma_{MRO/alass}$ is the MRO-glass interfacial energy. Because the MRO regions are viewed as defective Al crystals with no chemical difference between the MRO core and the Al crystal rim, there is an essentially low structural misfit at the MRO/crystal interface and complete wetting. Therefore, $\sigma_{MRO/glass}$ is regarded the

PLEASE CITE THIS ARTICLE AS DOI: 10.1063/5.0135730

same as $\sigma_{crystal/glass}$. Also $\sigma_{MRO/crystal}$ is estimated to be very small. Based on the interface energy of icosahedral quasicrystal/amorphous interfaces that are reported as $6\sim14$ (mJ/m²) 32,56 , $\sigma_{MRO/crystal}$ is estimated to be about 9 (mJ/m²). During crystallization, the MRO core with distorted Al-like order rearranges and merges into the nucleated nanocrystal (Fig. 6c) with negligible energy change. As noted in Fig. 6, the initial MRO/glass interface is replaced by the MRO/nanocrystal and nanocrystal/glass interfaces after crystallization. In order to further test the validity of heterogenous nucleation model, the homogeneous nucleation of Al crystals was calculated (Supplementary material E). From the calculation, homogeneous nucleation can not account for the nanocrystal number densities in the experimental temperature range due to the very low nucleation rate.



Fig. 6 (a) and (b) A schematic illustration of a nanocrystal nucleated on a disordered aluminum-like medium range order (MRO) region. The MRO/glass interface is replaced by the MRO/crystal interface. (c) The MRO rearranges and merges into the nanocrystal after nucleation.

The parameters used in Eq. 2 have been evaluated in order to determine predictions for the nucleation rate. The $\sigma_{crystal/glass}$ value is calculated to be $(0.16\pm0.003)\pm10^{-5}\text{T}$ (J/m²) through the method developed by Spaepen (Supplementary material A). The driving free energy, ΔG_{ν} based on the parallel tangent construction (Supplementary material B), is -1.0185×10⁶ (T-T_L) J/m³ within

PLEASE CITE THIS ARTICLE AS DOI: 10.1063/5.0135730

an error range of $(2.0941 \sim 0.8823) \times 10^6 \text{ J/m}^3$ where T_L is calculated as 860 ± 20 K. The r_0 value as 0.85 nm is obtained from FEM ³⁷.

Each of the evolving clusters will grow and shrink at a rate determined by the attachment frequency across the matrix/cluster interface:

$$\beta = \frac{1}{2Z^2\tau} \tag{3}$$

Where Z is the Zeldovich factor, τ is the delay time for nucleation and is defined as the time required to establish the steady-state nucleation in a system^{55,57,58}, which can be obtained from experiment.

By extrapolating the linear part of the particle number density vs. annealing time curve to intersect with the time axis (Fig. 4), the induction time θ can be obtained. The delay time τ is obtained by $\tau = 6\theta/\pi^2$ 56. The values of θ and τ at the four different temperatures are summarized in Table 1 Under the assumption that the delay time satisfies the Arrhenius relationship the temperature dependence of τ is given by

$$\tau = \tau_o \exp(Q/RT) \tag{4}$$

where Q is the activation energy governing atom attachment.

After fitting the discrete τ values at the four experimental temperatures, the continuous τ (T) could be obtained and plotted in Fig. 7. The activation energy Q obtained from the fitting is 3.28 ± 0.28 eV is within the range expected for diffusion in metallic glass ⁵⁹

Table 1 The induction time θ and the delay time τ at four temperatures.

T (°C)	237	240	245	247
θ (s)	1100 ± 150	640 ± 100	300 ± 70	180 ± 50
τ (s)	670 ± 90	389 ± 60	182 ± 42	110 ± 30

PLEASE CITE THIS ARTICLE AS DOI: 10.1063/5.0135730

Experimental data 3.5 Fitted delay time 3.0 log(r) 2.5 2.0 1.5 1.92 1.94 1.96 1.98 1.88 1.90 2.00 1/T (×10⁻³ 1/K)

Fig. 7 Relationship between temperature and delay time. The data points are experimental results. The line is the delay time fitted by an Arrhenius function.

4.2 Nucleation kinetics calculation

In order to test the MRO catalyzed nucleation model, a comparison was made between the experimental and model predicted values of the steady state nucleation rate (J_{ss}). The number and type of sites suitable for nucleation existing within the liquid must be identified to calculate the steady state nucleation rate. For the primary nucleation in Al-Y-Fe metallic glasses, the heterogeneous nucleation site is the MRO and the site density ρ is the volume density of MRO, which has been determined to be $(5.2 \pm 1) \times 10^{25}/m^3$ by FEM 37 . After substituting the parameter values into Eq. 1, the steady state nucleation rate is calculated as the curve in Fig. 8a. The calculated J_{ss} has a peak shape because at low temperatures, the nucleation is diffusion limited whereas at high temperatures, the nucleation is driving force limited. All the experimental J_{ss} data, obtained by measuring the slope of the linear part of the N_v vs. t_{anneal} plot (Fig. 4), lie on the lower temperature side of the peak because it is impossible to bypass the nose of the TTT (time-

PLEASE CITE THIS ARTICLE AS DOI: 10.1063/5.0135730

temperature-transformation) curve under the experimental heating rate in DSC (20 K/min). At the same time the high values for J_{ss} highlight the importance of the transient period to enable glass formation by rapid quenching. It is evident that extending the duration of the transient period is a key factor in promoting glass formation in bulk volumes. The volume term, V(t) in equation 5 is the volume fraction available for nucleation of a new crystal. As nucleation and growth occurs, the volume of material available for new nucleation is reduced. Ultimately, there is a reduction in the number of MRO sites. Inclusion of the V(t) term, which accounts for nucleation and growth (Supplementary material C), results in a saturation of the total number density of nucleated crystals. The good fit between the experimental results and the predicted values supports the nucleation model. An integration of the nucleation rate including the transient rate, J(t) yields the nanocrystal number density, N_{ν} as given by

$$N_{v} = \int_{0}^{t} J(t)V(t)dt = \int_{0}^{t} J_{SS}(T)exp\left(\frac{-\tau}{t}\right)V(t)dt$$
 (5)

The calculated N_{ν} values are plotted as the smooth curves in Fig. 4, which also show a good agreement with the experimental N_V data points. In addition, the multiplication of Eq. 3 and Eq.5 yields

$$ln(J_{SS}\tau) = ln(\frac{\rho}{2Z}) - (\frac{\Delta G^*}{kT}) \tag{6}$$

The value of Z as 0.01 is used to calculate the intercept $\ln(\rho/2Z)$ (supplementary material E). According to Fig. 8b, the fitted intercept value is 60.90±1.7, which is close to the calculated intercept $\ln(\rho/2Z) = 62$ and the fitted slope value is -0.89±0.12, which covers the calculated slope -1. The good fit also confirms the established nucleation model and indicates that a common mechanism is operating over the experimental range.

PLEASE CITE THIS ARTICLE AS DOI: 10.1063/5.0135730

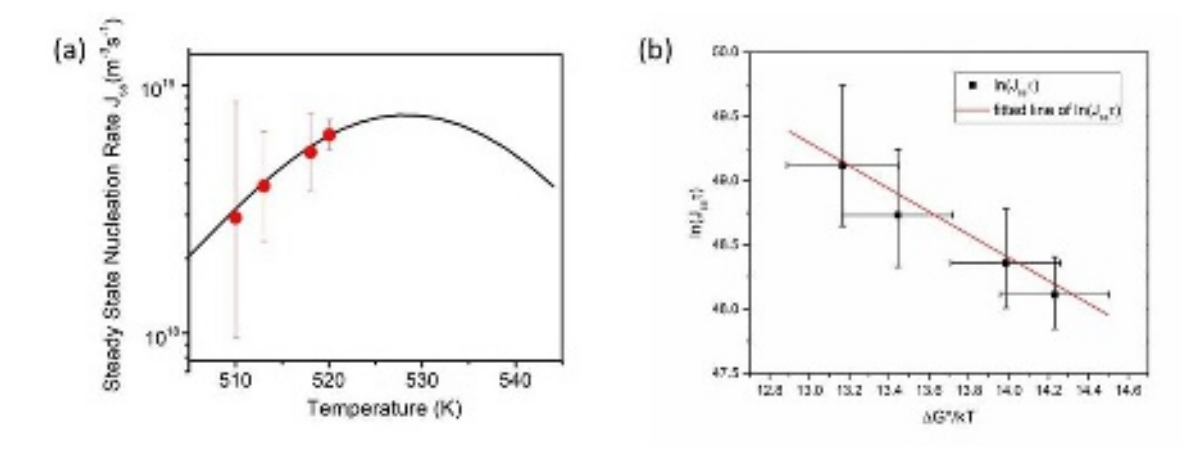


Fig. 8 (a) The calculated steady state nucleation rate (continuous curve) plotted together with the experimental J_{ss} (red data points), which is obtained by measuring the slope during the steady state stage in Figure 4. (b) $ln(J_{ss}\tau)$ vs. $\Delta G^*/kT$ relationship. The fitted intercept value is 60.90 ±1.69, which covers the calculated intercept $\ln(\rho/2Z) = 62$. The fitted slope value is -0.89±0.12, which is close to the calculated slope -1.

4.3 Nucleation model constraints

In order to further confirm the nucleation model, it is necessary to examine if the model can satisfy reasonable constraints on the parameter values used in the analysis. One important constraint concerns the value of σ_{LS} since it has a major impact on the nucleation kinetics. As pointed out by Cahn and Hilliard 60 , some of the earliest evaluations of σ_{LS} based upon droplet undercooling measurements do not satisfy the criterions $2\sigma_{LS} > \sigma_{gb}$ (σ_{gb} is the grain boundary energy) that is required to avoid the development of a liquid layer at grain boundaries. The reported experimental values for σ_{gb} for Al exhibit a range of values from 0.30 to 0.38 J/m2, but the values reported by Gündüz and Hunt⁶¹ based upon thermal groove measurements cover both σ_{LS} and σ_{gb} as $0.163 \pm 0.016 \text{ J/m}^2$ and $0.324 \pm 0.024 \text{ J/m}^2$ for Al-Cu and $0.169 \pm 0.024 \text{ J/m}^2$ and 0.336 ± 0.047 J/m² for Al-Si alloys respectively. In more recent computational analysis of σ_{LS} for a number of pure metals the resulting values were found to confirm the original Turnbull correlation expressed by $\sigma_{LS} = \alpha L \varphi^{2/3}$ where α is the Turnbull coefficient, L is the latent heat and φ is the number density

PLEASE CITE THIS ARTICLE AS DOI: 10.1063/5.0135730

of the crystal 62,63 . For FCC metals the computational analysis resulted in a modified α value of 0.55 that yields a σ_{LS} of about 0.15 J/m2 for Al which is close to the value from the Spaepen model. The experimental values for σ_{LS} are in good agreement with the σ_{LS} values calculated in this work and satisfy the σ_{gb}/σ_{LS} condition within the reported uncertainty range.

Second, at the metastable Al liquidus, the driving force ΔGv should be zero. The ΔGv value is zero at 860 K, which is the extrapolated liquidus temperature obtained from the Thermocalc software calculation (Supplementary material B). Third, the MRO radius r₀ should be smaller than the critical nucleation radius r*; otherwise, the MRO will be supercritical. Since r* decreases with temperature, if the r* at a lower temperature satisfies r*>r₀, then all the r* at a higher temperature will also be bigger than r₀. At 227 °C, which is 40 degrees lower than the T_x of Al₈₈Y₇Fe₅, r*(227 °C) is 0.9 nm and is larger than r₀ (0.85 nm). At extremely low annealing temperatures, even though the MRO is supercritical, the diffusion coefficient is so low that crystallization will be too slow for detection in a reasonable time period. Indeed, in an amorphous Als9Y6Fe5 alloy low temperature annealing required multiple days to weeks in order to initiate Al nanocrystal formation ⁶⁴. Fourth, the experimental J_{ss} data should fit with the calculated ones (Fig. 8). Fifth, $\Delta G^*/kT$ should be between 12 to 60 ⁵⁷ and according to the nucleation model, $\Delta G^*/kT$ is between 15 and 20, which is within the reasonable value range. Lastly, the atom jump frequency evaluated from the nucleation analysis has a correspondence with the atom jump frequency derived from diffusion measurements (supplementary material E).

5. Conclusions

Primary crystallization of amorphous alloys is an important pathway to the synthesis of nanoscale microstructures. Previous studies have indicated that amorphous Al alloys contain spatial heterogeneities composed of Al-rich regions exhibiting MRO. The heterogeneities can act This is the author's peer reviewed, accepted manuscript. However, the online version of record will be different from this version once it has been copyedited and typeset.

PLEASE CITE THIS ARTICLE AS DOI: 10.1063/5.0135730

as a catalyst to promote a high density of Al nanocrystals. From the quantitative structural analysis, a nucleation model has been developed for the MRO catalysis of Al nanocrystals that is based upon Al nucleating around the MRO core to lower the nucleation barrier. With the MRO seeded nucleation model and the kinetic data from the delay time (τ) measurement, the evolution of the measured Al nanocrystal density (Nv) can be accounted for during the primary crystallization through the isothermal annealing treatments. Also, the predicted values of steady state nucleation rates (Jss) and the enthalpy ΔH at the onset crystallization temperature (Tx) given by the nucleation model are consistent with the experimental results. In addition, MRO seeded nucleation model has satisfied the constraints set by the thermodynamic, kinetic and structural parameters. The model reflects a generic scheme for the treatment of MRO mediated nucleation reactions which may be applied more broadly to nucleation in materials characterized by the presence of spatial heterogeneities.

Supplementary Materials

See supplementary materials for Liquid-solid interface energy, free energy evaluation, nucleation model calculation and details of FEM.

Acknowledgement

The support of the Office of Naval Research (N00014-20-1-2704) is gratefully acknowledged.

Data Availability Statement

Data available on request from the authors.

PLEASE CITE THIS ARTICLE AS DOI: 10.1063/5.0135730

References

- ¹ Y.H. Kim, A. Inoue, and T. Masumoto, Materials Transactions, JIM **31**, 747 (1990).
- ² A. Inoue, K. Ohtera, A.P. Tsai, and T. Masumoto, Jpn J Appl Phys **27**, L479 (1988).
- ³ M. Calin and U. Köster, Materials Science Forum **269–272**, 749 (1998).
- ⁴ M. Salehi, S.G. Shabestari, and S.M.A. Boutorabi, Materials Science and Engineering A **586**, 407 (2013).
- ⁵ J.H. Perepezko and S.D. Imhoff, J Alloys Compd **504**, (2010).
- ⁶ H. Chen, Y. He, G.J. Shiflet, and S.J. Poon, Scripta Metallurgica et Materiala **25**, 1421 (1991).
- ⁷ M.C. Gao, F. Guo, S.J. Poon, and G.J. Shiflet, Materials Science and Engineering A **485**, 532 (2008).
- ⁸ J.J. Yi, L.T. Kong, M. Ferry, C.G. Tang, G. Sha, and J.F. Li, Mater Charact **178**, (2021).
- ⁹ J. Antonowicz, M. Kedzierski, E. Jezierska, J. Latuch, A.R. Yavari, L. Greer, P. Panine, and M. Sztucki, J Alloys Compd 483, 116 (2009).
- ¹⁰ A.K. Gangopadhyay, T.K. Croat, and K.F. Kelton, Acta Mater **48**, 4035 (2000).
- ¹¹ K.K. Sahu, N.A. Mauro, L. Longstreth-Spoor, D. Saha, Z. Nussinov, M.K. Miller, and K.F. Kelton, Acta Mater 58, 4199 (2010).
- ¹² J.C. Foley, D.R. Allen, and J.H. Perepezko, Scr Mater **35**, 655 (1996).
- ¹³ G. Wilde, H. Sieber, and J.H. Perepezko, Scr Mater **40**, 779 (1999).
- ¹⁴ K. Nakazato, Y. Kawamura, A.P. Tsai, A. Inoue, and T. Masumoto, Appl Phys Lett **63**, 2644 (1993).
- ¹⁵ S. Trady, M. Mazroui, A. Hasnaoui, and K. Saadouni, J Alloys Compd **744**, 750 (2018).
- ¹⁶ Y. Shen and J.H. Perepezko, J Alloys Compd **707**, 3 (2017).
- ¹⁷ D. v. Louzguine and A. Inoue, Mater Lett **54**, 75 (2002).
- ¹⁸ D. v. Louzguine-Luzgin and A. Inoue, Materials Science and Engineering A **448–451**, 1026 (2007).
- ¹⁹ B. Gu and F. Liu, Acta Mater **112**, 94 (2016).
- ²⁰ W. Li, L.T. Kong, and J.F. Li, Mater Charact **194**, (2022).
- ²¹ M.D.H. Lay, A.J. Hill, P.G. Saksida, M.A. Gibson, and T.J. Bastow, Acta Mater **60**, 79 (2012).
- ²² F. Li, X.J. Liu, H.Y. Hou, G. Chen, and G.L. Chen, J Appl Phys **110**, (2011).
- ²³ D. Moroni, P.R. ten Wolde, and P.G. Bolhuis, Phys Rev Lett **94**, (2005).



This is the author's peer reviewed, accepted manuscript. However, the online version of record will be different from this version once it has been copyedited and typeset.

PLEASE CITE THIS ARTICLE AS DOI: 10.1063/5.0135730

- ²⁴ B.S. Lee, G.W. Burr, R.M. Shelby, S. Raoux, C.T. Rettner, S.N. Bogle, K. Darmawikarta, S.G. Bishop, and J.R. Abelson, Science (1979) **326**, 980 (2009).
- ²⁵ J.H. Li, Y. Dai, Y.Y. Cui, and B.X. Liu, Materials Science and Engineering R: Reports **72**, 1 (2011).
- ²⁶ W.D. Liu, H.H. Ruan, and L.C. Zhang, Acta Mater **61**, 6050 (2013).
- ²⁷ S. Menon, G. Díaz Leines, R. Drautz, and J. Rogal, Journal of Chemical Physics **153**, (2020).
- ²⁸ G. Díaz Leines, A. Michaelides, and J. Rogal, Faraday Discuss **235**, 406 (2021).
- ²⁹ M. Fitzner, G.C. Sosso, F. Pietrucci, S. Pipolo, and A. Michaelides, Nat Commun **8**, (2017).
- ³⁰ E.D. Zanotto and M. Montazerian, Front Phys **8**, (2020).
- ³¹ G.C. Sosso, J. Chen, S.J. Cox, M. Fitzner, P. Pedevilla, A. Zen, and A. Michaelides, Chem Rev **116**, 7078 (2016).
- ³² G.W. Lee, Y.C. Cho, B. Lee, and K.F. Kelton, Phys Rev B **95**, (2017).
- ³³ Y. Sun, Y. Zhang, F. Zhang, Z. Ye, Z. Ding, C.Z. Wang, and K.M. Ho, J Appl Phys **120**, (2016).
- ³⁴ L. Zhao, G.B. Bokas, J.H. Perepezko, and I. Szlufarska, Acta Mater **142**, 1 (2018).
- ³⁵ W.G. Stratton, J. Hamann, J.H. Perepezko, P.M. Voyles, X. Mao, and S. v. Khare, Appl Phys Lett **86**, 1 (2005).
- ³⁶ F. Yi and P.M. Voyles, Ultramicroscopy **122**, 37 (2012).
- ³⁷ F. Yi, S.D. Imhoff, J.H. Perepezko, and P.M. Voyles, (2023).
- ³⁸ D. v. Louzguine and A. Inoue, J Mater Res **17**, 1014 (2002).
- ³⁹ D. v. Louzguine-Luzgin and A. Inoue, J Alloys Compd **399**, 78 (2005).
- ⁴⁰ Z.H. Huang, J.F. Li, Q.L. Rao, and Y.H. Zhou, Materials Science and Engineering A **489**, 380 (2008).
- ⁴¹ R. Lück, K. Lu, and W. Frantz, Scripta Metallurgica et Materiala **28**, 1071 (1993).
- ⁴² P.K. Gupta, D.R. Cassar, and E.D. Zanotto, Journal of Chemical Physics **145**, (2016).
- ⁴³ E.M. Pouget, P.H.H. Bomans, J.A.C.M. Goos, P.M. Frederik, G. de With, and N.A.J.M. Sommerdijk, Science (1979) **323**, 1455 (2009).
- ⁴⁴ D. Gebauer, A. Völkel, and H. Cölfen, Science (1979) **322**, 1819 (2008).
- ⁴⁵ W.J.E.M. Habraken, J. Tao, L.J. Brylka, H. Friedrich, L. Bertinetti, A.S. Schenk, A. Verch, V. Dmitrovic, P.H.H. Bomans, P.M. Frederik, J. Laven, P. van der Schoot, B. Aichmayer, G. de With, J.J. DeYoreo, and N.A.J.M. Sommerdijk, Nat Commun **4**, (2013).

This is the author's peer reviewed, accepted manuscript. However, the online version of record will be different from this version once it has been copyedited and typeset.

PLEASE CITE THIS ARTICLE AS DOI: 10.1063/5.0135730

- 46 A.L. Greer and K.F. Kelton, Journal of the American Ceramic Society **74**, 1015 (1991).
- ⁴⁷ J.W.P. Schmelzer, J Non Cryst Solids **354**, 269 (2008).
- ⁴⁸ J. Bokeloh, R.E. Rozas, J. Horbach, and G. Wilde, Phys Rev Lett **107**, (2011).
- ⁴⁹ D.T. Schweiss, J. Hwang, and P.M. Voyles, Ultramicroscopy **124**, 6 (2013).
- ⁵⁰ D.R. Allen, J.C. Foley, and J.H. Perepezko, Acta Mater **46**, 431 (1998).
- ⁵¹ Y.X. Zhuang, J.Z. Jiang, Z.G. Lin, M. Mezouar, W. Crichton, and A. Inoue, Appl Phys Lett **79**, 743 (2001).
- ⁵² T. Demirtaş and Y.E. Kalay, J Non Cryst Solids **378**, 71 (2013).
- ⁵³ H. Nitsche, F. Sommer, and E.J. Mittemeijer, Metall Mater Trans A Phys Metall Mater Sci **37**, 621 (2006).
- ⁵⁴ F. Spaepen, Solid State Physics Advances in Research and Applications **47**, 1 (1994).
- ⁵⁵ K.F. (Kenneth F.) Kelton and A.L. (Alan L. Greer, *Nucleation in Condensed Matter : Applications in Materials and Biology* (Elsevier, Oxford, 2010).
- ⁵⁶ Y.T. Shen, T.H. Kim, A.K. Gangopadhyay, and K.F. Kelton, Phys Rev Lett **102**, (2009).
- ⁵⁷ K.C. Russell, Adv Colloid Interface Sci **13**, 205 (1980).
- ⁵⁸ K.F. Kelton, Solid State Physics Advances in Research and Applications **45**, 75 (1991).
- ⁵⁹ F. Faupel, W. Frank, M.P. Macht, H. Mehrer, V. Naundorf, K. Rätzke, H.R. Schober, S.K. Sharma, and H. Teichler, Rev Mod Phys **75**, 237 (2003).
- ⁶⁰ J.E. Hilliard and J.W. Cahn, Acta Metallurgica **6**, 772 (1958).
- ⁶¹ M. Gündüz and J.D. Hunt, Acta Metallurgica **33**, 1651 (1985).
- ⁶² J.J. Hoyt, M. Asta, T. Haxhimali, A. Karma, R.E. Napolitano, R. Trivedi, B.B. Laird, and J.R. Morris, MRS Bull **29**, 935 (2004).
- ⁶³ D.Y. Sun, M. Asta, J.J. Hoyt, M.I. Mendelev, and D.J. Srolovitz, Phys Rev B Condens Matter Phys **69**, (2004).
- ⁶⁴ J. Bokeloh, N. Boucharat, H. Rösner, and G. Wilde, Acta Mater **58**, 3919 (2010).

